Coherent structure analysis of cavitation waterjets using dynamic mode decomposition

Zhenlong Fang(方珍龙)[1,2,3,4], Wenjiang Hou(侯文江)[1,2,3], Shidong Fan(范世东)[1,2,3], Xiaofeng Guo(郭孝峰)[4], Yong Chen（陈勇）[1,2,3, a)]

AFFILIATIONS

[1] State Key Laboratory of Maritime Technology and Safety, Wuhan University of Technology, Wuhan 430063, China
[2] Sanya Science and Education Innovation Park of Wuhan University of Technology, Sanya 572025, China
[3] School of Transportation and Logistics Engineering, Wuhan University of Technology, Wuhan 430063, China
[4] LIED, UMR 8236, CNRS, Université Paris Cité, F-75006 Paris, France
a) Author to whom correspondence should be addressed: yongchen@whut.edu.cn

ABSTRACT

This study analyzes the influence of nozzle geometry on the vortex and cavitation cloud structures. The differences between the coherent structures of the Helmholtz nozzle, organ pipe nozzle, and venturi nozzle jets are investigated through large eddy simulation. The vorticity transport equation is used to investigate the relationship between the cavitation cloud and diagonal pressure torque terms. The cavitation and vortex structure shedding frequencies of the jets are investigated using the dynamic mode decomposition method. Three distinct stages of the cavitation bubbles are illustrated: priming, expansion, and collapse. The nozzle structure determines the shape of the primary cavitation bubbles. Moreover, turbulent kinetic energy convergence facilitates the maintenance of the coherent structure. Organ pipe nozzle jets have a high peak velocity at the center axis. Their vortex structure only exhibits a stretched state in the downstream and collapses later than the vortex structures of other nozzles. Advantageously, organ pipe nozzles maintain the stability of the coherent structure. The jets generated by the three nozzles have similar static modes. Helmholtz nozzles produce jets with higher energy and periodically shedding small-scale vortex structural modes. These modes are coupled to the static flow field, resulting in quasi-periodic oscillations of the Helmholtz nozzle jets. The periodic oscillation effect of the Helmholtz nozzle jets is superior to that of the other nozzle jets. The high-energy modes of the venturi nozzle jets have anisotropic and small-scale vortex structures. Furthermore, the venturi nozzle jets exhibit good dispersion and cavitation properties. This study provides guidance for the use of jets with different properties in the respective engineering fields.

I. INTRODUCTION

Water jet technology is widely researched due to its various advantages, such as ecofriendliness, energy conservation, and high efficiency. The cross application of water jet technology with other fields has hastened its development. Various water jet technologies exist that meet most engineering requirements in the fields of cleaning[1, 2], cutting[3,4], engineering heat transfer[5, 6, 7], material testing[8, 9], and drilling[10].

Several investigations have been conducted to improve the jet efficiency. Studies have determined that the nozzle structure affects the jet energy conversion efficiency. Variations in the nozzle structure cause significant changes in the performance parameters, such as flow velocity, pressure, and agglomeration in the flow fields of the water jets. The vortex structure of oscillation jets differs from that of continuous jets (FIG. 1).

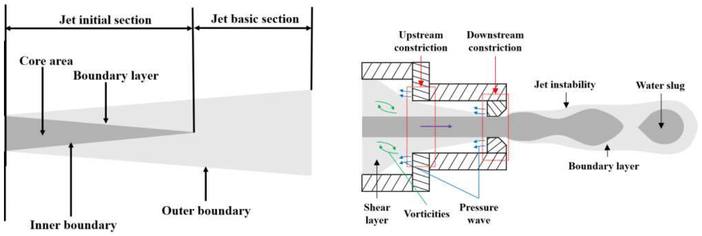

FIG. 1. Schematic of a continuous jet (left) and a pulsed jet (right)[11].

The research on self-excited oscillation jets has focused on two main aspects. First, in experimental investigations, the turbulent structure and cavitation characteristics are directly observed using high-speed photography technology and measurements. Second, dynamic data are extracted through numerical simulations to quantitatively analyze the oscillation properties and coherent structure of jets. Shi *et al.*[12] optimized the exit aspect ratio of an organ pipe nozzle and analyzed the axial pressure oscillation characteristics of the jet, improving the organ pipe nozzle jet performance. Nie *et al.*[13] predicted the gas precipitation performance of self-excited oscillating cavities using a heuristic prediction algorithm. They obtained the parameter intervals for which the self-excited oscillatory cavities maintained good gas precipitation performance. Cai *et al.*[14] added active excitation to the cavitation jets, and they determined that the synergy between strong passive excitation and harmonized frequency with active excitation resulted in the most robust cavitation cloud development. Li *et al.*[15] optimized the organ pipe nozzle structure to obtain the optimal inlet pressure and cavity length of self-resonant nozzles by targeting the Strouhal number. Wu *et al.*[16] combined high-speed photography and image processing procedures to extract the coherent structures of cavitation cloud shedding. They determined that the length and period of the cavitation cloud of oscillation jets are significantly influenced by variations in the cavity length, cavity diameter, and pressure ratio. Presenting an overview about the recent advances in experimental and numerical studies of cavitating venturi, Vijayan *et al.*[17] summarized the predictability limits of popularly used mixture models coupled with cavitation and turbulence. Moreover, Yuan *et al.*[18] proposed a modified model to predict the lock-on frequency based on fluid networks and vibration analysis and found that the oscillations were more significant when the standing waves in the cavity interacted with the shedding vortex. By investigating the frequency spectra and flow characteristics of self-excited oscillation pulsed jets, Fang *et al.*[19] discovered that the Helmholtz oscillator influences jets through feedback modulation. Further research has illustrated that the flow inside a Helmholtz chamber can be divided into three stages, which depict a close relationship between the vortex–cavitation interaction and the flow mechanism[20]. Thus, changes in the cavity structural parameters significantly impact the magnitude of pressure fluctuations. Shi *et al.*[21] conducted numerical simulations and erosion experiments of composite structure nozzles by combining Helmholtz and organ pipe nozzles and obtained the optimal nozzle parameters. Research has shown that composite nozzles have more significant pressure amplitude and better cleaning effect than individual nozzles. Wang *et al.*[22] conducted an experimental study on the pressure oscillation characteristics of organ pipe and Helmholtz composite nozzles. The results yielded the optimum geometric parameters and target distance. Yuan *et al.*[23] proposed a composite nozzle with a venturi tube and Helmholtz resonator. They obtained and analyzed the outlet pressure pulsation frequencies through fast Fourier transform. The results showed that the composite nozzle increases the dominant frequency of the pressure oscillations. Using the schlieren technique, Qin *et al.*[24] investigated the evolution of compressible vortex rings produced by a shock-tube apparatus with three nozzle geometries. They discovered that the diverging nozzle yields larger vortex rings with lower propagation velocities but produces fewer and more turbulent trailing jets. Cheng *et al.*[25] established a water jet cavitation model by introducing the water pressure of the jets into the Keller–Miksis equation. The model considers the sound interaction among bubbles. The jet test verified that the water jet velocity and pressure difference at the nozzle entrance and exit significantly influence the evolution of cavitation bubbles. Dong *et al.*[26] simulated the jet flow of an angular nozzle using computational fluid dynamics (CFD). The cavitation jet generated by an angular nozzle presents a vortex ring structure. The expansion section of an angular nozzle is the low-pressure area of the fluid where cavitation bubbles are generated and developed. Furthermore, the jet penetration, width, spreading angle, and shedding frequency are closely related to the hydrodynamic conditions. Chen *et al.*[27] proposed a hybrid algorithm for optimizing the angular nozzle geometry, focusing on the axial maximum volume fraction. They provided a new research direction for improving the performance of cavitation jets.

Ahn *et al.*[28] investigated the flow and aeroacoustics of twin square jets by implicit large-eddy simulations, and the coupling mode of the twin jets was determined as the symmetrical flapping mode. Cheng *et al.*[29] used the LES method combined with the Schnerr–Sauer cavitation model to simulate tip leakage cavitating flow. The vorticity transport equation was then used to further analyze the influence of the cavitation on the vortices. Long *et al.*[30] used implicitly filtered Large Eddy Simulation with a homogenous cavitation model to investigate the transient turbulent cavitating flow around a Clark-Y hydrofoil. The numerical results also reveal that the periodic cavity shedding causes the complex and turbulent flow feature by vortex and spectrum analyses. Wang *et al.*[31] used homogeneous mixture model to capture the macroscopic vapor structures, while the microbubble behavior was tracked by Lagrangian model. This method was then used to analyze the cloud cavitation evolution mechanism and the internal cavity structure. Two different bubble generation mechanisms were proposed to explain the bubble size distribution spectra in the unsteady cavitating flow. Cheng *et al.* [32] summarized the cavitation in tip-leakage flow and its control, and some advanced topics for the future work are suggested to further promote the study of the tip-leakage vortex cavitation.

Data-driven analysis methods can extract evolution characteristics through the corresponding modes. The dynamic mode decomposition (DMD) method is data-driven and spatiotemporal decoupled. It is widely used in fluid dynamic studies containing abundant spatiotemporal coupled data. The DMD method can yield eigenfrequencies that are difficult to capture via conventional methods. Liu *et al.*[33, 34], Han *et al.*[35], and Liu *et al.*[36] conducted a series of DMD analysis on cavitation flows for various geometries, such as hydrofoils, impeller, and pumps, and provided practically beneficial techniques for understanding cavitation flows. These studies employed different rules to select the dominant flow modes, which play crucial roles in constructing low-dimensional dynamic models for prediction and reconstruction. Hu *et al.*[37] conducted a series of visualization experiments of the cavitation clouds in the nozzle chamber. The proper orthogonal decomposition (POD) method provides the cavitation modulation mechanism of self-excited oscillation pulsed jets. Peng *et al.*[38] conducted high-speed visualization experiments and analyzed the periodicity of a cavitation cloud using the POD method. They uncovered that the cavitation intensity can be increased by adding microparticles. Sinha *et al.*[39] investigated the liquid jet breakup in the presence of crossflow and analyzed the results obtained from the high-speed visualization using the POD method for jet stability probing. They determined that the shape of the jet oscillating chamber significantly affects the jet stability. Xu *et al.*[40] investigated the different morphologies and distributions of cavitation clouds using the POD method. They effectively extracted the spatiotemporal characteristics of cavitation clouds in water jets and found that the mode of organ pipe nozzles has many large structures with wide and long cavitation clouds. The POD method is effective for detecting that the cavitation flow structure generated by the venturi tube mainly comprises the re-entrant jet that flows upstream (Mode 1) and large rotating eddies downstream (Mode 2). The re-entrant jet structure in the cloud cavity is much larger than that in the sheet cavity, and the energy predominance of mode 1 in the cloud cavity is more significant than that in the sheet cavity[41]. The coherent structures of POD and DMD for the inertial and thermal modes comprise counter-rotating structures. The DMD algorithm can consistently extract the characteristic frequency for a single attached cavity process[42]. Ge *et al.*[43] used particle image velocimetry measurements and DMD for flow structure investigations in the entire cavitation area. They found that the DMD method can effectively extract the reverse flow in the jet, which has a predominant energy ratio that leads to the Kelvin–Helmholtz instability.

The cavitation flow field is coupled by many flow structures at different scales. Most researchers directly analyzed the cavitation cloud, vortex, and other structures generated by the cavitation flow and neglected the spatiotemporal coupling characteristics. This study analyzes the interaction between the cavitation and coherent structure in combination with the vorticity transport equation. Furthermore, the reduced-order decomposition of dominant coherent structures is investigated using DMD to effectively extract the jet energy dominant modes, thus determining whether the jet energy is decaying or growing. The dominant dynamical characteristics of oscillating cavitation flows need to be analyzed and the interaction between turbulent coherent structure and cavitation properties in self-excited oscillation jets need to be elucidated.

II. NUMERICAL APPROACH

A. Geometrical setup and boundary conditions

FIG. 2 presents the shape and specific dimensions of the three types of oscillating nozzles considered in this study. TABLE I lists the detailed parameters of the three nozzles. The upstream jet enters from the circular nozzle in the middle of the upstream impingement wall and outflows from the downstream nozzle. The inlet and outlet are properly prolonged to ensure the full development of the jet and attain high convergence accuracy. The Reynolds number of the flow is based on the upstream nozzle diameter: d_1 is fixed to 2.6 mm herein. The length of the upstream pipe L_i is used to adjust the nozzle size such that the three kinds of nozzles have the same outlet position. The organ pipe nozzle has a stepped shape. Jets are fully developed before they enter the chamber. To minimize the number of grids and ensure the flow field is fully developed, the length and diameter of the external flow field are set as 70 and 40 mm, respectively.

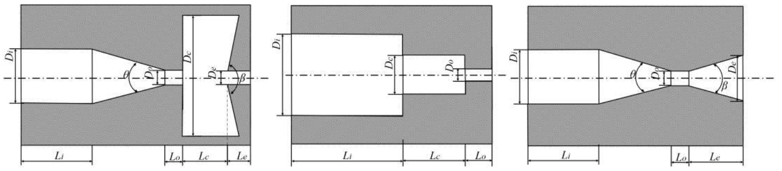

FIG. 2. Schematic of the three nozzles.

TABLE I. Geometric parameters of the nozzles

Nozzle type	D_i(mm)	D_o(mm)	D_e/D_o	L_c/D_o	D_c/D_o	L_o/D_o	**θ(°)**	**β(°)**
Helmholtz nozzle	3.5	2.6	1.2	2	8	3	13.5	120
Organ pipe Nozzle	6.5	2.6	/	8	2.6	3	/	/
Conical Nozzle	6.5	2.6	/	/	/	3	13.5	/
Venturi Nozzle	6.5	2.6	3	/	/	3	13.5	30

The simulation is conducted using the three-dimensional (3D) ANSYS FLUENT 15.0 code. The large eddy simulation (LES) model is used for turbulence simulation.

The control equations employed herein are described in a previous work. Fang *et al.*[20] used the LES model for cavitation jet simulation and found that the LES model can well capture the coherent structure. Hence, this study selects the mixture multiphase flow model and the Zwart–Gerber–Belamri (ZGB) cavitation model. Additionally, the numerical simulation of the cavitation jet flow field is conducted using the sublattice model of Wall-Adapting Local Eddy-Viscosity (WALE). The WALE constant is taken as 0.325. The numerical selection and solution strategy are illustrated in TABLE II. The following boundary conditions are used: the impingement walls, sidewalls, and pipe walls have no-slip conditions, while the inlet and outlet boundaries are both pressure boundaries. A uniform flow profile is adopted at the entrance, and the turbulence intensity for the incoming flow is set as 3%.

TABLE II. Numerical scheme.

Grid	Staggered grid
Pressure–velocity coupling algorithm	Coupled
Multiphase model	Mixture
SGS model	WALE
Viscous terms	Bounded central differencing
Time discretization	Second-order implicit
Time step size, Δt	5×10^{-6}

B. Parameter setting

Gridding is conducted based on the groundwork of the computational domain. Significant grids are needed to discern the fluctuation in the inertial subrange. Figure 3 depicts the 3D model. The finite volume mesh is entirely composed of hexahedrons, and the value of y+ is approximately equal to 1.0.

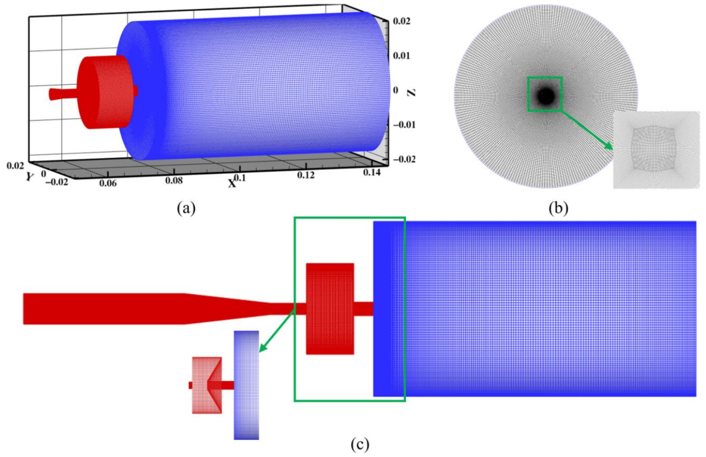

(a)

(b)

(c)

FIG. 3. (a) 3D mesh view, (b) grid distribution in the XZ plane, and (c) grid distribution in the XY plane. (Helmholtz nozzle as an example)

Mesh refinement is used in the area near the wall and inside the chamber. Take the Helmholtz nozzle as an example. Figure 4 depicts the mesh independency. When the pressure at the nozzle outlet is 2 MPa, the average of the peaks and valleys of 20 consecutive fluctuations is taken as the index for the grid-independence validation. The error between the grid numbers of 9.14×10^6 and 1.04×10^7 is determined to be negligible. Thus, the grid number 9.14×10^6 is used to conduct the subsequent research.

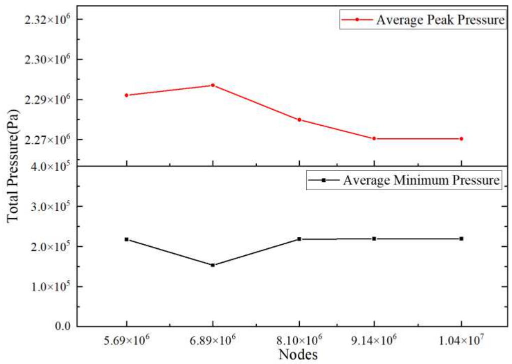

FIG. 4. Results of the mesh independence for the Helmholtz oscillator (P_{inlet} = 2 MPa)

When the operating pressure P_{inlet} = 2 MPa, the average of the peaks of 20 consecutive waveforms is taken to obtain the average maximum pressure during the test. As shown in FIG. 5, the Helmholtz nozzle exhibits strong oscillatory characteristics.

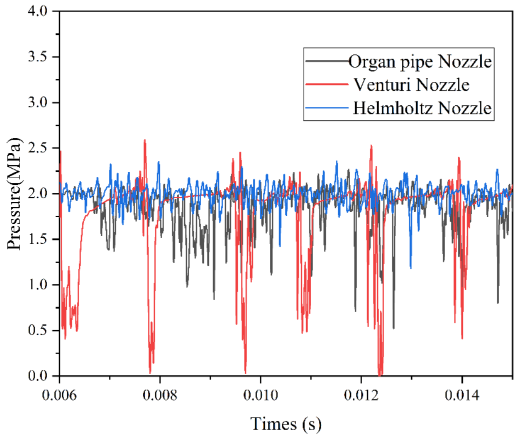

FIG. 5. Pressure pulsation of nozzle exit.

When P_{inlet} is varied from 1.0 to 2.5 MPa, the peak average of 20 consecutive crests is taken to obtain the average maximum pressure. Table III presents the comparison of the obtained results with the numerical results. The experimental data obtained at the maximum pressure are 10% higher than the CFD data[20]. When the orifice loss is considered, the error is even smaller. Considering the non-constant behavior of the cavitation flow, this error is acceptable.

TABLE III. Comparison of the exit pressure of the Helmholtz nozzle obtained through the experiment and CFD.

Operating Pressure [MPa]	Exp. Data [MPa]	CFD Data [MPa]	Error (%)
1.0	1.485	1.263	14.94
1.5	2.091	1.745	16.54
2.0	2.529	2.272	10.24
2.5	2.992	2.693	10.00

FIG. 5 depicts the results of the numerical simulation at the nozzle outlet. The peak pressure pulsation at the nozzle outlet is about 2.5 MPa when $P_{inlet} = 2$ MPa. The power spectral density of the Helmholtz nozzle pressure oscillation is given in FIG. 6 and is predicted to follow the −5/3 power law in the range of inertia subrange, indicating that the −5/3 power law of the pressure spectra is predicted by the grid numbers of 9.14×10^6.

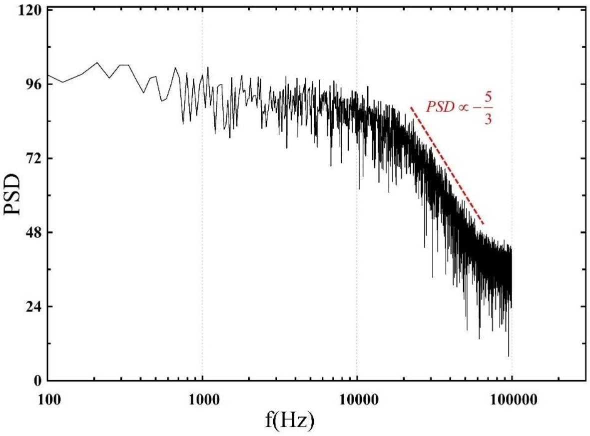

FIG. 6. Pressure spectrum at cavity outlet

C. Model validation

Fang *et al.*[20] performed experiments to capture snapshots of the cavitation cloud in the Helmholtz nozzle jet. The upstream nozzle diameter was D_o=2.6mm, viz. D_e/D_o = 1.2 (diameter ratio), L_c/D_o = 2 (length ratio), and D_c/D_o = 8 (contraction ratio). The experimental operating pressure was P_{inlet} = 2 MPa. Pressure pulsations at the nozzle outlet were collected. In this simulation, the structural parameters and operational conditions were identical to the settings in the experiments.

The comparison between the experimental patterns and numerical snapshots of cavity development within one typical cycle is shown in FIG. 7. Experimental comparison with the original snapshots from previous high-speed photography of jets. *T* denotes the cavity development period by the experiments and simulation, and the same label *T* is used in FIG. 7 for convenience. The agreement between the experimental observations and simulation results indicates that the LES model can capture the essential features of the cloud cavitation phenomenon. At $t_1 = 1/4T$, agglomeration occurs among the tiny bubbles at the nozzle outlet, which initiates a downstream flow process that is marked by the expansion of the bubbles. This expansion is driven by the decrease of the saturated vapor pressure. The periodicity of the cavitation bubbles produced by the nozzle is clearly visible at $t_2 = 1/2T$. The shape of the labeled cavitation bubbles changes due to the vorticity and viscosity stretching effect. FIG. 7 illustrates the collapse of the cavitation structure due to energy dissipation at $t_3 = 3/4T$. The entire process of the cavitation structure from initial bubble generation until collapse is depicted in FIG. 7.

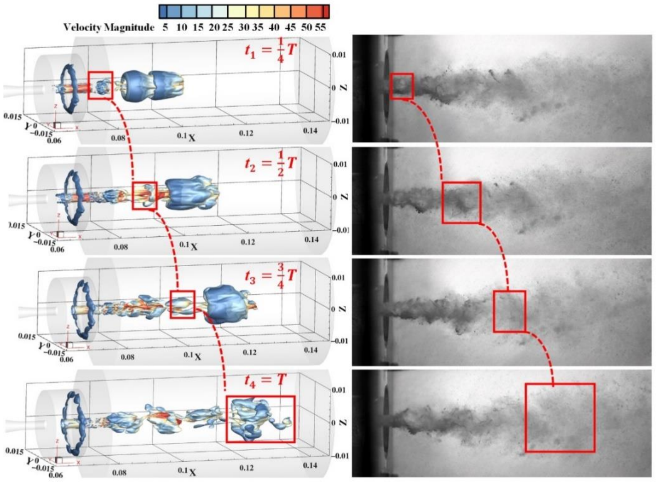

FIG. 7. Experimental and numerical comparison of the cavitation cloud evolution, $P_{inlet} = 2$ MPa. (a) Numerical cavitation pattern by 25% vapor volume fraction iso-surface. (b) Exp. Results.

D. DMD method

After the numerical simulation, a matrix of *N* moments of the flow field snapshot sequences $X=\left[x_1\ x_2\ x_3\ \ldots x_N\ \right]$ is obtained, where the time interval *Δt* between two adjacent snapshots x_i of the flow field data is small. The vectors x_{i+1} and x_i are linearly mapped:

$$x_{i+1}=Ax_i \tag{1}$$

where *A* is a high-dimensional matrix.

The number of spatial location points *M* of the flow field data snapshot *XI* is considerably larger than that of snapshot sequences N. *A* is an M × M high-dimensional matrix, and a reduced approximation matrix $\tilde{A}$ of *A* can be obtained to estimate the eigen parameters.

Two sub-matrices are constructed: $X_1^{N-1}=\left[x_1\ x_2\ x_3\ \ldots x_{N-1}\ \right]$ and $X_2^N=\left[x_2\ x_3\ x_4\ \ldots x_N\ \right]$. The combination of these sub-matrices with Eq. (1) yields

$$\begin{gathered}X_2^N=\left[x_2\ x_3\ x_4\ \ldots x_N\ \right]= \\ \left[Ax_1\ Ax_2\ \ldots Ax_{N-1}\ \right]=AX_1^{N-1}\end{gathered} \tag{2}$$

$$X_1^{N-1}=U\Sigma V^* \tag{3}$$

$$A\approx U\tilde{A}U^* \tag{4}$$

where *U* represents the left singular matrix, Σ denotes the singular value diagonal matrix, and *V** and *U** are the complex conjugate transpose matrices of *V* and *U*, respectively.

Using Eq. (3), the singular value decomposition of X_1^{N-1} is performed. The optimal low-dimensional approximation matrix $\tilde{A}$ of *A* is obtained through the matrix similarity principle described in Eq. (4).

$$\tilde{A} = U^{*} X_2^{N} V \Sigma^{-1} \tag{5}$$

Eq. (5) produces the diagonal matrix *Λ* comprising eigenvalues λ_i of $\tilde{A}$ and the matrix *W* comprising eigenvectors ξ_i of $\tilde{A}$.

Subsequently, the logarithm is taken of the eigenvalues of λ_i, the i_{th} mode corresponding to the growth/decay rate σ_i, and the phase velocity ω_i containing the mode frequency information:

$$\frac{\ln \lambda_i}{\Delta t} = \sigma_i + j\omega_i = \frac{\ln|\lambda_i|}{\Delta t} + j\frac{\arg \lambda_i}{\Delta t} \tag{6}$$

The frequency is

$$f_i = \frac{\omega_i}{2\pi} \tag{7}$$

III. RESULTS AND DISCUSSION

A. Cavitation characterization of flow

The distribution of the root mean squared error of the velocities (RMSE velocity) at different distances from the outlet to the outflow field is shown in FIG. 8. D_O is the diameter of the nozzle outlet, and the distribution of the monitor line is discretized. The root mean square error (RMSE) is a metric employed to gauge the accuracy of continuous data. The root mean square error (RMSE) quantifies the square root of the average squared difference between the observed values and the predicted values. FIG. 9(a) presents the kinetic energy dissipation due to the strong oscillation characteristics at the near-nozzle exit and the cavitation occurrence. Therefore, the velocity at the axis is lower than that at the nozzle exit radius position. Venturi tube nozzle jets exhibit a slow velocity drop along the y-axis, showing great jet dispersibility due to the divergence angle and velocity anisotropy. The Helmholtz nozzle jets demonstrate the fastest velocity drop along the y-axis, indicating that the strong pressure oscillations result in the dissipation of kinetic energy. The organ pipe nozzle jet maintains the maximum axial velocity in all positions and well retains the energy.

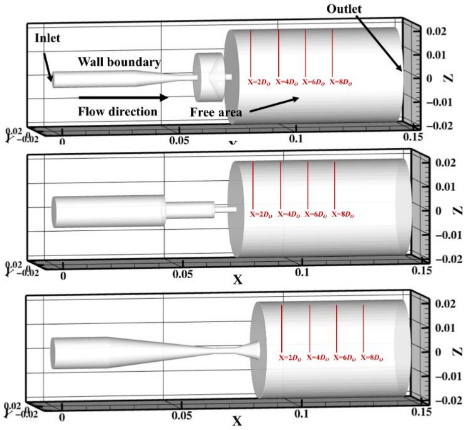

FIG. 8. Computational domain and detection line placement.

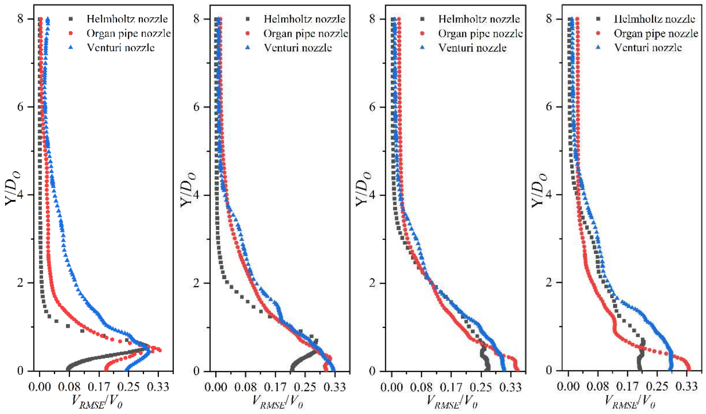

(a) (b) (c) (d)

FIG. 9. Velocity distribution at different monitored lines in the outflow field (a) X

= $2D_o$, (b) X = $4D_o$, (c) X = $6D_o$, and (d) X = $8D_o$. V_{RMSE} is the root mean square error of the velocity. V_0 is the mean velocity at the nozzle outlet.

FIG. 10 illustrates the initial cavitation bubbles generated by the different nozzle configurations, where cavitation initially occurs near the downstream nozzle of the Helmholtz oscillator (FIG. 7). Cavitation bubbles are constrained by impingement wall and formed within the Helmholtz oscillation cavity, i.e., the unrestrained development of cavitation is suppressed. The development of a cavitating vortex ring within a cavity illustrates complex vortex wall collisions. This leads to the near-wall bubble breakup and generation of microjets that influence the subsequent cavitation process. The vapor volume fraction within the cavity exhibits periodic variations, which results in the periodic shedding of cavitation bubbles, especially those observed at the nozzle outlet. The cavitation bubbles generated by the Helmholtz nozzle possess a circular shape (FIG. 10(a)). Organ pipe nozzles generate cavitation bubbles that have an elliptical shape with pointed tips (FIG. 10(b)). Venturi nozzles generate cavitation bubbles with a spindle-like shape (FIG. 10(c)).

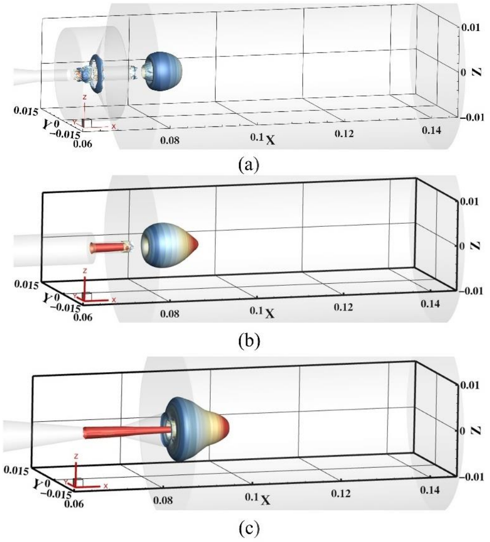

FIG. 10. Numerical cavitation bubbles produced by different nozzles with a 25% vapor volume fraction iso-surface. (a) Primary cavitation bubbles produced by the Helmholtz nozzle. (b) Primary cavitation bubbles generated by the organ pipe nozzle. (c) Primary cavitation bubbles yielded by the venturi nozzle.

B. Research on the coherent structure

The iso-surface $Q = 1 \times 10^8$ is selected to assess the vortex structure evolution over time, as illustrated in FIG. 11. The shedding process of the Kelvin–Helmholtz vortex is repeatedly observed near the Helmholtz oscillation cavity entrance. At $t_1 = 1/4T$, the vortex ring within the chamber moves downstream as it expands and disperses, exhibiting a disordered state. When the vortex ring reaches the nozzle outlet, the pressure suddenly decreases, which leads to the jet volume expansion, causing the vortex to chaotical develop and forming a horseshoe vortex. At $t_2 = 1/2T$, the upstream horseshoe vortex ring stretches as the flow progresses downstream, which leads to the volume expansion of the coherent structure. Figure 11 illustrates the entire process of a vortex ring separating from the main frequency, stretching, and collapsing. Comparison of the turbulent kinetic energy shows that the vortex structure is more compact in regions with higher turbulent kinetic energy, suggesting that the jet energy concentration is beneficial for maintaining the vortex coherent structure.

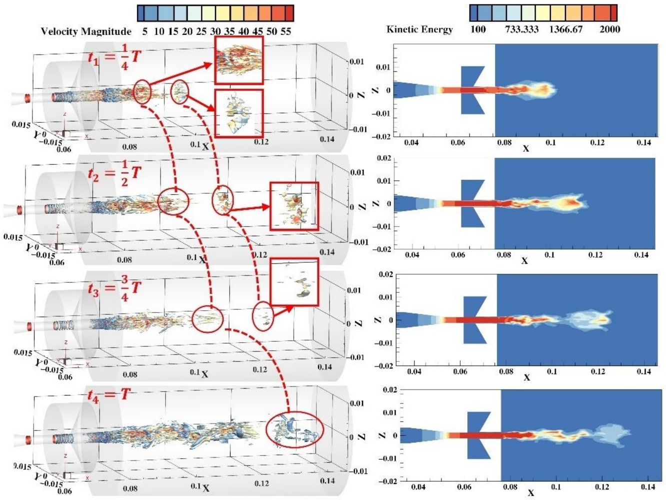

(a) (b)

FIG. 11. Vortex structures and kinetic comparison of cavitation cloud evolution. (a) Vortex structures by iso-surface of $Q = 1 \times 10^8$. (b) turbulent kinetic energy map.

FIG. 12 describes the vortices generated by the three nozzles after the jet stabilizes. FIG. 12(a) illustrates the typical properties of the coherent structure in the Helmholtz self-excited oscillation jet. In the upstream, a horseshoe vortex is generated, which undergoes a process of stretching and collapsing as it moves downstream. As shown in FIG. 12(b), vortex disturbances are generated near the shear layer of the organ pipe

PLEASE CITE THIS ARTICLE AS DOI: 10.1063/5.0197532

nozzle outlet. In the high volume fraction region, the vortex structure experiences a significant stretching effect. As depicted by FIG. 9, high kinetic energy is beneficial for maintaining the vortex structure. The venturi nozzle jets exhibit chaotic small-scale vortex structure priming in the divergence angle. Moreover, the downstream flow field region exhibits significant vortex structure collapse, as shown in FIG. 12(c).

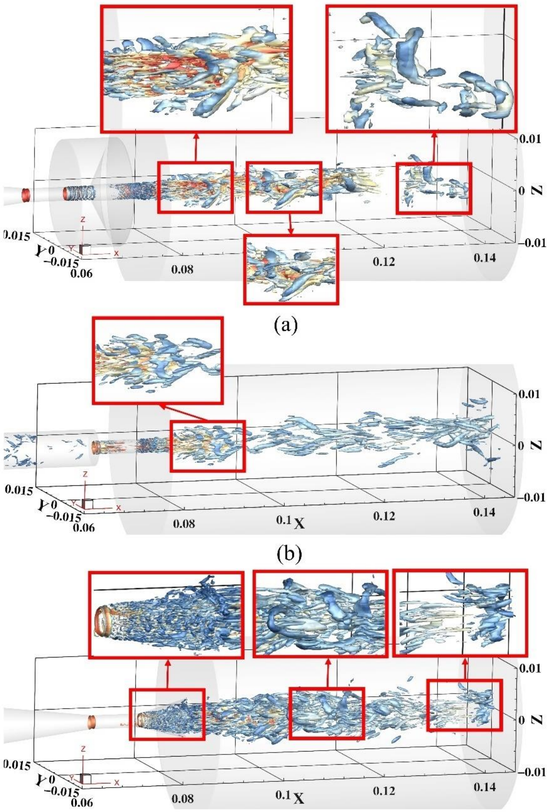

(a)

(b)

(c)

FIG. 12. Simulated vortex structures embodied by the iso-surface of Q = 1 × 10^8 in steady flow. $P_{inlet} = 2$ MPa. (a) Helmholtz nozzle. (b) Organ pipe nozzles. (c) Venturi nozzles.

C. Study of vortex transportation equations

To explore the vortex–cavitation interaction mechanism, the vorticity transport equation in variable density flow is applied to the turbulent flow.

$$\frac{D\omega_z}{Dt} = [(\vec{\omega}\cdot\nabla)\vec{V}]_z - [\vec{\omega}(\nabla\cdot\vec{V})]_z + \left[\frac{\nabla\rho_m \times \nabla p}{{\rho_m}^2}\right]_z + [(\upsilon_m + v_t)\nabla^2\vec{\omega}]_z \tag{8}$$

Here, the term on left-hand side is the rate of vorticity change due to fluid flow. On the right-hand side, the first term is the vortex stretching term, which mainly stems from the velocity gradient; the second term is the vortex dilatation term, which mainly arises from the fluid volume variation and characterizes the effect of fluid compressibility on the vorticity; the third term is the baroclinic torque (due to the misaligned pressure and density gradient); and the last term is the rate of vorticity change due to the viscous diffusion of the vorticity, as the viscous diffusion term has little effect on the vorticity.

FIG. 13 presents the nephograms illustrating the vapor volume fraction, vortex stretching term, vortex dilatation term, and diagonal pressure torque term for a typical cycle. At t_1 = 1/4T, these three terms exhibit distinct vorticity transport levels, with the vortex stretching term prominently influencing the Helmholtz oscillation cavity. At the oscillator near-wall exit, the vortex stretching is distributed along the exit wall and is mainly influenced by the velocity gradient. The vortex stretching term at t_2 = 1/2T and t_3 = 3/4T is considerably more significant than that at t_1 = 1/4T. This increase is attributed to the rapid change in the local density. The vortex expansion term is equal to zero in regions where no volumetric expansion or contraction occurs, especially in non-cavitation regions.

Cavitation originates in the Helmholtz oscillator and propagates throughout the flow field. During this expansion, the oblique pressure torque plays a significant role in inducing vorticity. In Fig. 13(c) and (d), sharp cavitation fluctuations play a crucial role in promoting the coupling of vortex structures. Near the vapor-liquid interface, the cavity structure experiences instability. During the expansion phase of the cavity, the diagonal pressure torque term manifests in positive and negative pairs. This suggests that the density gradient and pressure gradient within the bubbles have different directions, a result of the divergence of density and pressure gradients in this context.

In a circulation flow field, pronounced and dynamic mass exchange consistently occurs at the vapor–liquid boundary. The formation of the eccentric torque is related to the deviation of the surface viscous forces of the microfluid from the centroid of the fluid. the existence of diagonal pressure torque implies that the viscous forces can generate a vortex inside the flow field. The diagonal pressure torque term is influenced by both the pressure and density. Consequently, this torque is distributed along the cavitation bubble edges, providing a rough depiction of the vapor volume fraction contours. Although the diagonal pressure torque term may not be as prominent as the vortex stretch and expansion terms, its importance should not be underestimated. Ji *et al.*[44] stated that it could be the primary mechanism behind cavitation vortex formation. These results demonstrate a strong connection between cavitation and vortices. Further exploration in future studies could reveal more details and mechanisms.

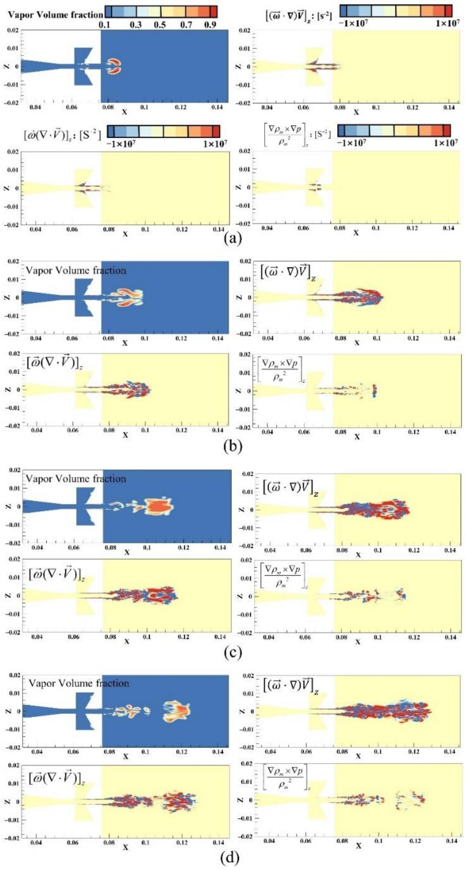

FIG. 13. The simulation vapor volume fraction, vortex stretching term, vortex dilatation, and baroclinic torque term in one typical cycle. $P_{\text{inlet}} = 2$ MPa. (a) $t_1 = \frac{1}{4}T$. (b) $t_2 = \frac{1}{2}T$. (c) $t_3 = \frac{3}{4}T$. (d) $t_4 = T$.

FIG. 14 illustrates the nephograms depicting the vapor volume fraction, vortex stretch, vortex expansion, and oblique pressure torque terms for the three types of typical nozzles at $t_4 = T$. The vortex stretching and vortex dilatation remain the dominant vortex structures in the three typical jets. The negligible effect of the jet produced by the Helmholtz nozzle on the vorticity is mainly attributed to the periodic development of the cavitation bubbles. Affected by the large-scale cavitation bubbles, the jets generated by the organ pipe and venturi nozzles exhibit small values for the vortex extension term upstream. The Helmholtz nozzle exhibits the highest value for the vortex stretching term, implying that the production of large-scale cavitation bubbles has an inhibitory effect on the vortex stretching term.

The nephograms profile of the diagonal pressure torque term aligns with the vapor volume fraction cloud profile. The mass exchange occurring in the vapor–liquid phase is closely related to the pressure torque term due to the significant mass exchange that occurs at the vapor volume fraction cloud boundary. This exchange leads to a change in the density gradient, which consequently affects the oblique pressure torque.

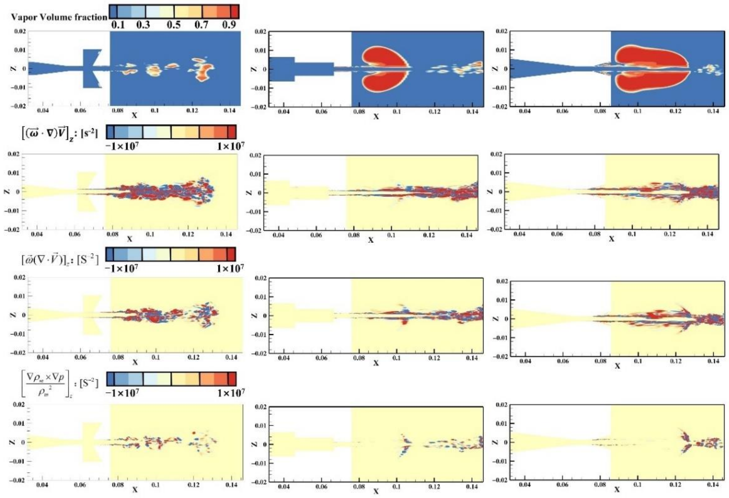

(a) (b) (c)

FIG. 14. The vapor volume fraction, vortex stretching term, vortex dilatation, and

baroclinic torque term at $t_4 = T$ and $P_{inlet} = 2$ MPa. (a) Helmholtz nozzle. (b) Organ pipe nozzle. (c) Venturi nozzle.

D. DMD method for analyzing the jet flow

Typical flow field data are extracted after steady flow field calculations. The eigenvalue distributions are obtained by processing the external flow field data generated by the Helmholtz nozzle with the DMD method. FIG. 15(a) illustrates the modal eigenvalues entering the quasi-periodic phase. FIG. 15(b) depicts the relationship between the real and imaginary parts of the logarithmic eigenvalues.

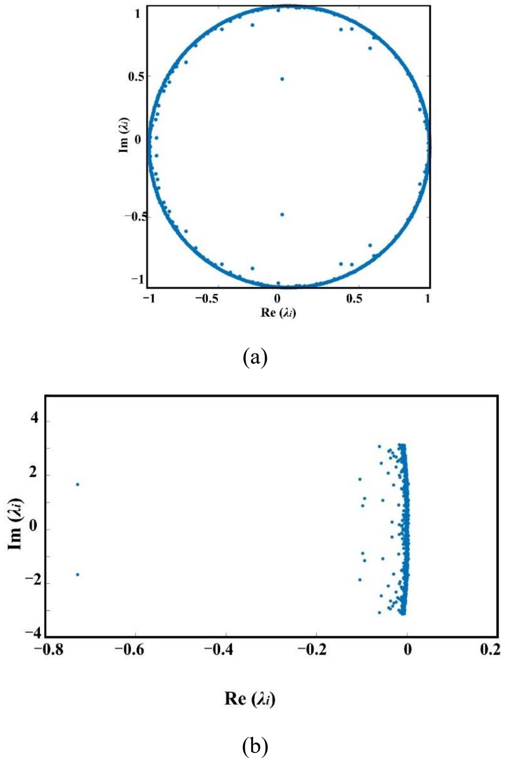

(a)

(b)

FIG. 15. Eigenvalues and logarithmic eigenvalues for the real part of the

eigenvalues. (a) Eigenvalues. (b) Logarithmic eigenvalues.

Modes with eigenvalues occurring in pairs as conjugate modes essentially represent a single mode with identical dynamics. Most modes are located within and very close to the unit circle. This implies that most of the patterns are weakly stabilized during the developmental stage, depicting a gradual decay process. A few modes are present on the unit circle, suggesting the existence of a limited number of limit-stable periodic cyclic modes during the developmental stage. FIG. 15(b) shows that some modes have $\sigma_i > 0$, indicating that the modes are dispersed. The modal energies are arranged in descending order. Since the conjugate modes essentially represent a single mode, only one of them is analyzed.

The total energy percentage by the first i_{th} mode and the energy percentage occupied by the i_{th} modes are defined as follows:

$$\begin{aligned} & I_{pp}(1:i) = \left(\sum_{i=1}^{N} I_i / \sum_{i=1}^{R} I_i\right) \times 100\%, \\ & N = 1, 2, \ldots, R \end{aligned} \tag{9}$$

$$I_{pp}(i) = I_i / \sum_{i=1}^{R} I_i \tag{10}$$

where R represents the total number of remaining modes after the elimination of one of the conjugate modes.

Figure 16 illustrates the total energy percentage by the first i_{th} mode in comparison to the energy percentage occupied by the i_{th} modes. During the development stage, the initial 10 orders of the extracted main modes contribute to more than 20% of the energy ratio.

TABLE IV lists the corresponding kinetic parameters. The value of the imaginary eigenvector of Re (λ_i) and the frequency of the 6th mode (f_i) are both zero. This mode is considered static and represents the average flow field characteristics over the sampling time period. It does not change with time and contributes to an energy percentage of approximately 1.2%. In TABLE IV, the 2_{th}, 3_{th}, 4_{th}, 5_{th}, 6_{th}, and 7_{th} order modes have positive σ, indicating that these modes are stable features of the divergence property. The parameter σ is associated with the dynamic system stability. In this case, positive σ values denote the stable behavior of these patterns, with divergence properties related to the evolution of the system over time. The first-order mode represented by σ has the largest energy contribution and is characterized by a negative value, suggesting that the mode exhibits stable behavior and decay characteristics. Using the DMD method, the modal frequency with the highest energy percentage is measured to be 2483 Hz. The ordering of the energy share in the modal divergence and convergence seems to be mixed, reflecting a nonlinear developmental process within the jet flow field.

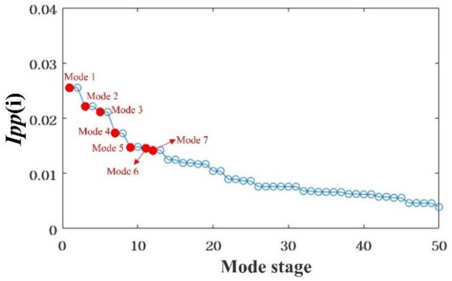

(a)

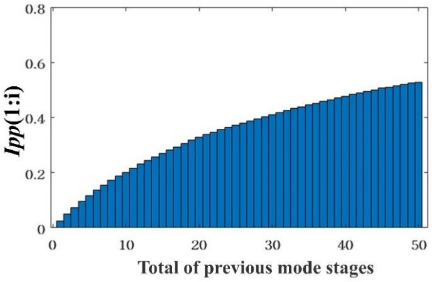

(b)

FIG. 16. The energy percentage of the i_{th} mode. and the total energy of the first i_{th} mode. (a) The total energy of the first i_{th} mode. (b) The energy percentage of the i_{th} mode.

TABLE IV. Dynamical parameters for i_{th} modes (Helmholtz nozzle)

Mode	Re λ_i	Im λ_i	σ_i	f_i/Hz	g_i
1	0.995	0.0247	−6.8595	2483	−468
2	0.9388	0.2658	55.8730	27595	−2459
3	0.9794	0.1256	15.5335	12751	−1263
4	0.9351	−0.3250	8.2585	−33453	−1012
5	0.9325	−0.3294	27.7195	−33956	−1110
6	1	0	25.8681	0	42
7	0.9792	−0.1552	21.1465	−15721	−861

FIG. 17 displays the modal plots of the energy distribution ratios sorted to the first seven orders obtained by processing the vapor volume fraction data with DMD. The 6_{th} order mode represents a static mode, indicating that the mean flow field remains constant with time. This reflects the main characteristic of the flow field. The 1^{st} order modes with the highest energy percentage are mainly influenced by small-scale bubbles near the nozzle. Moreover, these modes exhibit the shedding of the downstream large-scale bubbles, identifying them as the main coherent structures responsible for the quasi-periodic cavitation phenomenon at the nozzle. As the modal order increases, the contained energy and the vapor structure size decrease. Additionally, small-scale vortex shedding begins to dominate, with a gradual increase in the shedding frequency and a significant increase in the number of bubbles.

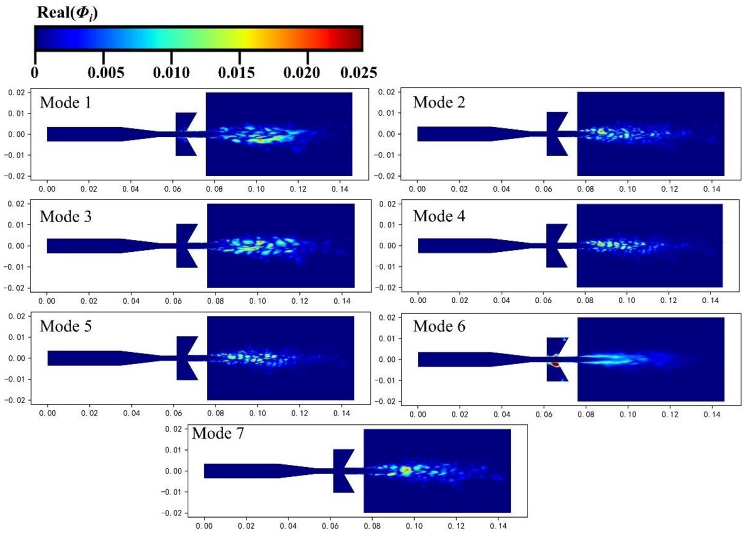

FIG. 17. Modal plots of the energy distribution ratios sorted to the first seven orders obtained by processing the vapor volume fraction data with DMD. Helmholtz nozzle

FIG. 18 presents the modal plots of the energy distribution ratios sorted to the first five orders obtained by processing the vapor volume fraction data with DMD. In the figure, the second-order modal statistics in the left column and fifth-order modal statics in the right column are the static modes of the organ pipe and venturi nozzles, respectively, demonstrating large-scale bubble shedding in the flow field upstream. All other modes exhibit small-scale discrete bubble shedding. The contained energy and the vapor structure size decrease with increasing modal order. The venturi nozzle still exhibits a significant cavitation structure downstream, indicating its good cavitation performance. This is in contrast to the Helmholtz cavitation jet characteristics, for which no significant shedding was observed.

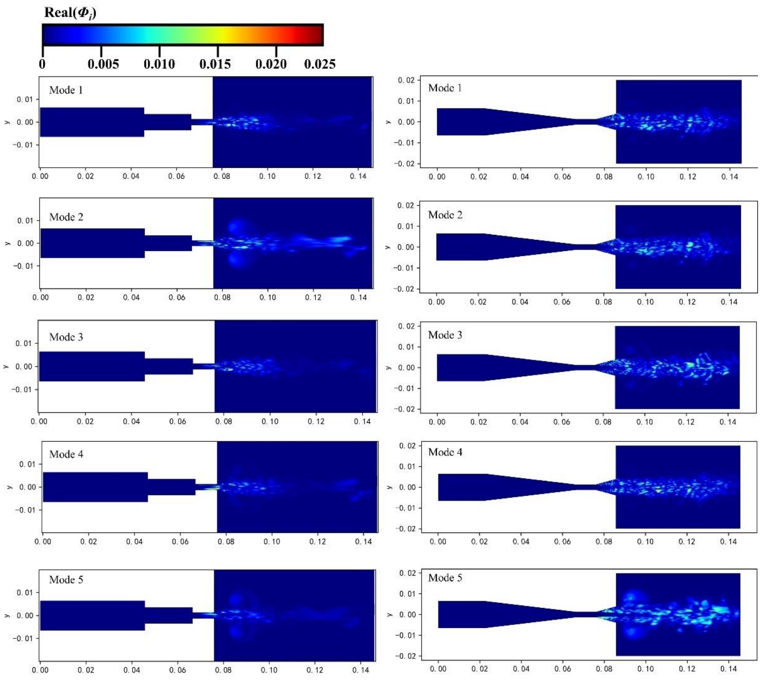

(a) (b)

FIG. 18. Modal plots of the energy distribution ratios sorted to the first five orders obtained by processing the vapor volume fraction data with DMD. (a) Organ pipe nozzle. (b) Venturi nozzle

Wu *et al.*[45] captured the coherent structure of the cloud cavitation flow field using the finite-time Lyapunov exponent method and the reduced-order modeling method. As the upstream-ordered vortex ring progresses downstream and interacts with the wall, it generates secondary and tertiary vortices. These vortices affect the ordered vortices. The interactions between vortex-vortex and vortex-wall cause the vortex ring to periodically expand and break along the collision wall. The vortex structure inside the oscillator, combined with the periodic variation of the vapor-phase volume fraction, produces a pulsating pressure field. This pulsating pressure field creates an effective jet drive at the same frequency as the inlet-ordered flow. The jet shear layer responds to the jet driving force and amplifies it in its intrinsic frequency range. The ordered portion of the jet is strengthened, and the ordered discrete vortex rings move outward into the flow field, generating a self-excited oscillation phenomenon with periodic pulsations.

FIG. 19 displays the modal plots of the energy distribution ratios sorted to the first five orders obtained by processing the vorticity data with DMD. The vorticity data are obtained from the simulations of the Helmholtz nozzle, organ pipe nozzle, and venturi nozzle. In the first-order self-excited oscillatory modes generated by the Helmholtz nozzle, the circumferentially aligned vortices interact with the cavitation structures. This effect leads to the entrainment of the coherent structure to the surrounding ambient fluids. The generation of small-scale perturbations of all orders embedded in the large-scale vortex results in the existence of multiplicative frequency harmonics of all orders in the self-sustained oscillations. The static flow of Helmholtz nozzle jets is in the 4^{th} mode. Oscillating jets generated by the Helmholtz nozzle exhibit significant periodic vortex shedding in the 2^{nd} and 5^{th} modes. The comparison reveals that the jet vortices produced by the venturi and organ pipe nozzles have a finer and more disordered structural scale than those produced by the Helmholtz nozzle. These theoretical results are consistent with the conclusions obtained from previous treatments of organ pipe nozzle jets[46]. The static modes of the three types of nozzles are highly similar and all occur at the exit boundary layer, indicating that the main contributor to the difference in the flow characteristics is the flow field coupled with small-scale periodic vortex shedding.

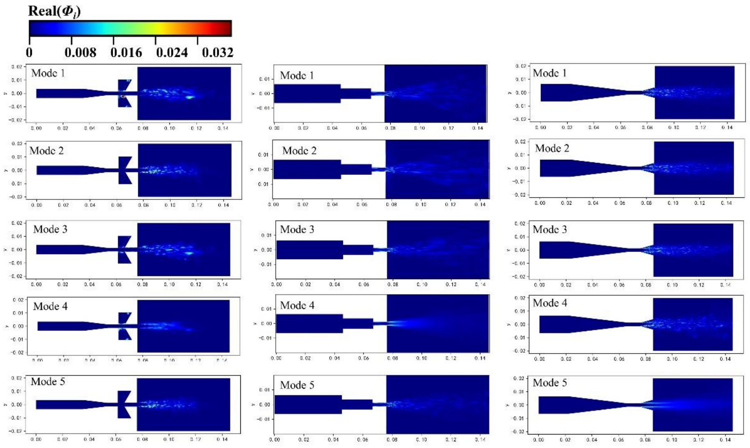

(a) (b) (c)

FIG. 19. Modal plots of the energy distribution ratios sorted to the first five orders obtained by processing the vorticity data with DMD. (a) Helmholtz nozzle. (b) Organ pipe nozzle. (c) Venturi nozzle

IV. CONCLUSION

This study conducted numerical simulation of the 3D turbulent cavitation flow in three types of nozzles using the LES method. The numerical calculation results closely matched the available experimental data, validating the accuracy and reliability of our computational models. The following conclusions were obtained:

(1) Three distinct stages of cavitation bubbles were illustrated: priming, expansion, and collapse. The shape of the primary cavitation bubbles was dependent on the nozzle structure. The cavitation bubbles generated by the Helmholtz nozzle exhibited a circular shape. The cavitation bubbles generated by the organ pipe nozzle had an elliptical shape with pointed tips. The venturi nozzle generated cavitation bubbles with a spindle-like shape. The expansion of the cavitation bubbles was the main reason for the stretching of the coherent structure; the shedding of the vortex ring from the jets' main frequency was accompanied by the expansion and collapse of cavitation bubbles.

(2) Turbulent kinetic energy convergence facilitated the maintenance of the coherent structure. Organ pipe nozzle jets had a high peak velocity at the center axis. The vortex structure of the organ pipe nozzle jets only exhibited a stretched state in the downstream and collapsed later than that of the other nozzles. Thus, the organ pipe nozzle can advantageously maintain the stability of the coherent structure.

(3) DMD analysis revealed that the jets generated by the above nozzles had similar static modes. Helmholtz nozzles produce jets with higher energy and periodically shedding small-scale vortex structural modes. These modes were coupled to the static flow field, which caused the quasi-periodic oscillations of the Helmholtz nozzle jet. The periodic oscillation effect of the Helmholtz nozzle jets was superior to that of the other nozzle jets.

(4) The high-energy modes of the venturi nozzle jets exhibited anisotropic and small-scale vortex structures. Hence, the venturi nozzle jets had good dispersion and cavitation properties.

AUTHOR DECLARATIONS

Conflict of Interest

The authors have no conflicts to disclose.

Author Contributions

Zhenlong Fang: Funding acquisition (lead); Formal analysis (equal); Investigation (equal); Methodology (equal); Writing - original draft (equal). **Wenjiang Hou**: Conceptualization (equal); Formal analysis (lead); Investigation (lead); Methodology (lead); Software (lead); Validation(lead); Writing - original draft (lead); Writing – review & editing (equal). **Xiaofeng Guo**: Methodology (equal); Supervision (equal); Writing –review & editing (equal). **Shidong Fan**: Methodology (equal); Supervision (equal); Writing –review & editing (equal). **Yong Chen**: Conceptualization (lead); Formal analysis (equal); Investigation (equal); Methodology (equal), Writing –review & editing (equal).

DATA AVAILABILITY

The data that support the findings of this study are available from the corresponding author upon reasonable request.

Funding

This research was funded by the National Natural Science Foundation of China (grant number: 51706161， 52071240), Finance Science and Technology Project of Hainan Province (grant number: ZDKJ202015), China Scholarship Council (grant number 202006955016).

REFERENCES

1. L.-Y. Huang and Z. S. Chen, "Effect of technological parameters on hydrodynamic performance of ultra-high-pressure water-jet nozzle," Appl. Ocean Res. **129**, 103410 (2022).
2. Y. Yao, H. Wang, Z. Fang, D. Li and B. Wang, "Experimental study and prediction

model of the cleaning effect induced by self-resonating cavitating waterjet," J. Mech. Sci. Technol. **36**, 5097-5106 (2022).

3. Y.-P. Cao, S.-M. Cheng, W.-D. Shi, Y.-F. Yang and G.-W. Wang, "Experimental Study on Surface Erosion of Grade A Marine Steel by Ultrahigh-Pressure Water Jet," Water **14**, 1953 (2022).
4. S. Jasper, J. Hussong and R. Lindken, "PIV investigation of high Reynolds number submerged water jets at high-pressure ambient conditions," Exp. Fluids **62**, 97 (2021).
5. A. Liu, P. G. Talalay, X. Fan, Y. Yang, D. Gong and R. Wang, "Theoretical and numerical simulation research about annular nozzle parameters influence on heat transfer in hot-water ice-coring drilling," Case Studies in Thermal Engineering **47**, 103122 (2023).
6. M. Ge, M. Petkovšek, G. Zhang, D. Jacobs and O. Coutier-Delgosha, "Cavitation dynamics and thermodynamic effects at elevated temperatures in a small Venturi channel," International Journal of Heat and Mass Transfer **170**, 120970 (2021).
7. I. Piya, A. Kumar, N. Kaewchoothong and C. Nuntadusit, "Flow and heat transfer characteristics of submerged impinging air-water jets," International Journal of Thermal Sciences **193**, 108503 (2023).
8. O. Usta, Ç. S. Köksal and E. Korkut, "A systematic study into the cavitation erosion test for marine propeller materials by cavitating jet technique," Ocean Engineering **284**, 115252(2023).
9. D.-D. Zhuang, S.-H. Zhang, H.-X. Liu and J. Chen, "Cavitation erosion behavior and anti-cavitation erosion mechanism of NiTi alloys impacted by water jet," Wear **518-519**, 204631(2023).
10. C. Feng, Y. Wang and L. Kong, "Effects of pulsating fluid at nozzle inlet on the output characteristics of common and self-excited oscillation nozzle," Energy Science & Engineering **10**, 3189-3200 (2022).
11. Y. Chen, Z. Fang, T. Xiong, W. Hou, Z. Zhang and R. Shi, "An experimental study on the erosion of sandstone by self-excited oscillation cavitation waterjet in submerged environment," Ocean Engineering **279**, 114546(2023).
12. H. Shi, Y. Kang, D. Li and Z. Fang, "Effects of the exit aspect ratio of organ-pipe nozzle on the axial pressure oscillation characteristics of self-resonating waterjet," Proceedings of the Institution of Mechanical Engineers, Part C: Journal of Mechanical Engineering Science **234**, 4589-4598 (2020).
13. S. Nie, M. Li, H. Ji, F. Yin and Z. Ma, "Heuristic prediction of gas precipitation performance of self-excited oscillation cavity," Physics of Fluids 35, 085106 (2023).
14. T. Cai, Z. Wang, L. P. Chamorro, L. Zheng and F. Ma, "Cavitation cloud of waterjet under double excitation," Physics of Fluids 35, 111301 (2023).
15. D. Li, Y. Chen, Y. Kang, Z. A. Wang, X. Wang, Q. Fan and M. Yuan, "Experimental investigation of the preferred Strouhal number used in self-resonating pulsed waterjet," J. Mech. Sci. Technol. **32**, 4223-4229 (2018).
16. Q. Wu, W. Wei, B. Deng, P. Jiang, D. Li, M. Zhang and Z. Fang, "Dynamic characteristics of the cavitation clouds of submerged Helmholtz self-sustained

oscillation jets from high-speed photography," J. Mech. Sci. Technol. **33**, 621-630 (2019).

17. A. Vijayan and P. K. P, "Characterization of cavitation zone in cavitating venturi flows: Challenges and road ahead," Physics of Fluids 35, 123326 (2023).
18. M. Yuan, D. Li, Y. Kang, H. Shi and H. Pan, "Characteristics of Oscillation in Cavity of Helmholtz Nozzle Generating Self-excited Pulsed Waterjet," Chinese Journal of Mechanical Engineering **35**, 73 (2022).
19. Z. Fang, Q. Wu, M. Zhang, H. Liu, P. Jiang and D. Li, "Large Eddy Simulation of Self-Excited Oscillation Pulsed Jet (SEOPJ) Induced by a Helmholtz Oscillator in Underground Mining," Energies **12**, 2161(2019).
20. Z. Fang, F. Zeng, T. Xiong, W. Wei, P. Jiang, Q. Wu, Y. Wang and Y. Fei, "Large eddy simulation of self-excited oscillation inside Helmholtz oscillator," Int. J. Multiphase Flow **126**, 103253 (2020).
21. D. Shi, Y. Xing, L. Wang, Z. Chen and D. Adair, "Numerical Simulation and Experimental Research of Cavitation Jets in Dual-Chamber Self-Excited Oscillating Pulsed Nozzles," Shock and Vibration **2022**, 1-12 (2022).
22. X. Wang, Y. Li, Y. Hu, X. Ding, M. Xiang and D. Li, "An Experimental Study on the Jet Pressure Performance of Organ–Helmholtz (O-H), Self-Excited Oscillating Nozzles," Energies **13**, 367 (2020).
23. M. Yuan, D. Li, Y. Kang, H. Shi and Y. hu, "The Characteristics of Self-Resonating Jet Issuing from the Helmholtz Nozzle Combined with a Venturi Tube Structure," Journal of Applied Fluid Mechanics **13**, 779-791 (2020).
24. L. Qin, Y. Xiang, S. Qin and H. Liu, "On the structures of compressible vortex rings generated by the compressible starting jet from converging and diverging nozzles," Aerospace Science and Technology **106**, 106188 (2020).
25. F. Cheng, W. Ji, C. Qian and J. Xu, "Cavitation bubbles dynamics and cavitation erosion in water jet," Results in Physics **9**, 1585-1593 (2018).
26. W. Dong, L. Yao and W. Luo, "Numerical Simulation of Flow Field of Submerged Angular Cavitation Nozzle," Applied Sciences **13**, 613(2023).
27. Y. Chen, Y. Hu and S. Zhang, "Structure optimization of submerged water jet cavitating nozzle with a hybrid algorithm," Engineering Applications of Computational Fluid Mechanics **13**, 591-608 (2019).
28. M. Ahn, M. Mihaescu, A. Karnam, E. Gutmark, "Large-eddy simulations of flow and aeroacoustics of twin square jets including turbulence tripping," Physics of Fluids **35**, 066105(2023).
29. H. Cheng, X. Bai, X. Long, B. Ji, X. Peng and M. Farhat, "Large eddy simulation of the tip-leakage cavitating flow with an insight on how cavitation influences vorticity and turbulence," Appl. Math. Modell. **77**, 788-809 (2020).
30. Y. Long, X. Long, B. Ji and T. Xing, "Verification and validation of Large Eddy Simulation of attached cavitating flow around a Clark-Y hydrofoil," Int. J. Multiphase Flow **115**, 93-107 (2019).
31. Z. Wang, H. Cheng, B. Ji and X. Peng, "Numerical investigation of inner structure and its formation mechanism of cloud cavitating flow," Int. J. Multiphase Flow **165**, 104484 (2023).

32. H. Cheng, B. Ji, X. Long, W. Huai and M. Farhat, "A review of cavitation in tip-leakage flow and its control," J. Hydrodyn. **33**, 226-242 (2021).
33. M. Liu, L. Tan and S. Cao, "Dynamic mode decomposition of gas-liquid flow in a rotodynamic multiphase pump," Renewable Energy **139**, 1159-1175 (2019).
34. M. Liu, L. Tan and S. Cao, "Method of dynamic mode decomposition and reconstruction with application to a three-stage multiphase pump," Energy **208**, 118343 (2020).
35. Y. Han and L. Tan, "Dynamic mode decomposition and reconstruction of tip leakage vortex in a mixed flow pump as turbine at pump mode," Renewable Energy **155**, 725-734 (2020).
36. Y. Liu, Q. Wu, B. Huang, H. Zhang, W. Liang and G. Wang, "Decomposition of unsteady sheet/cloud cavitation dynamics in fluid-structure interaction via POD and DMD methods," Int. J. Multiphase Flow **142**, 103690(2021).
37. J. Hu, M. Yuan, G. Feng, X. Wang and D. Li, "Experimental investigation on the cavitation modulation mechanism in submerged self-sustained oscillating jets," Ocean Engineering **274**, 114108(2023).
38. C. Peng, S. Tian, G. Li and M. Wei, "Enhancement of cavitation intensity and erosion ability of submerged cavitation jet by adding micro-particles," Ocean Engineering **209**, 107516 (2020).
39. A. Sinha, "Effect of injector geometry in breakup of liquid jet in crossflow – insights from POD," Int. J. Multiphase Flow **167**, 104497 (2023).
40. Y. Xu, H. Liu, Z. Wang, J. Zhang and J. Wang, "Analysis of the Effects of Nozzle Geometry on the Cavitation Water Jet Flow Field Using Orthogonal Decomposition," Iranian Journal of Science and Technology, Transactions of Mechanical Engineering **023**, 00647 (2023).
41. M. Ge, G. Zhang, M. Petkovšek, K. Long and O. Coutier-Delgosha, "Intensity and regimes changing of hydrodynamic cavitation considering temperature effects," Journal of Cleaner Production **338**, 130470 (2022).
42. W. Liang, T. Chen, G. Wang and B. Huang, "Investigation of unsteady liquid nitrogen cavitating flows with special emphasis on the vortex structures using mode decomposition methods," International Journal of Heat and Mass Transfer **157**, 119880 (2020).
43. M. Ge, P. Manikkam, J. Ghossein, R. Kumar Subramanian, O. Coutier-Delgosha and G. Zhang, "Dynamic mode decomposition to classify cavitating flow regimes induced by thermodynamic effects," Energy **254**, 124426 (2022).
44. Y. Long, X. Long, B. Ji and T. Xing, "Verification and validation of Large Eddy Simulation of attached cavitating flow around a Clark-Y hydrofoil," Int. J. Multiphase Flow **115**, 93-107 (2019).
45. Y. Wu, R. Tao, Z. Yao, R. Xiao and F. Wang, "Analysis of low-order modal coherent structures in cavitation flow field based on dynamic mode decomposition and finite-time Lyapunov exponent," Physics of Fluids **35**, 085110 (2023).
46. Z. Fang, W. Hou, Z. Xu, X. Guo, Z. Zhang, R. Shi, Y. Yao and Y. Chen, "Large Eddy Simulation of Cavitation Jets from an Organ-Pipe Nozzle: The Influence of Cavitation on the Vortex Coherent Structure," Processes **11**, 2460 (2023).